MASS CYCLING THROUGH CRUSTAL MAGMA CHAMBERS AND THE INFLUENCE OF THERMO-MECHANICAL STATE ON MAGMA COMPOSITIONS THROUGH TIME

by

CONSTANCE OZIMEK

A THESIS

Presented to the Department of Earth Sciences
and the Graduate School of the University of Oregon
in partial fulfillment of the requirements
for the degree of
Master of Science

September 2017

THESIS APPROVAL PAGE

Student: Constance Ozimek

Title: Mass Cycling through Crustal Magma Chambers and the Influence of Thermo-Mechanical State on Magma Compositions through Time

This thesis has been accepted and approved in partial fulfillment of the requirements for the Master of Science degree in the Department of Earth Sciences by:

Leif Karlstrom	Chair
Paul Wallace	Member
Thomas Giachetti	Member

and

Sara D. Hodges	Interim Vice Provost and Dean of the Graduate School

Original approval signatures are on file with the University of Oregon Graduate School.

Degree awarded September 2017

THESIS ABSTRACT

Constance Ozimek

Master of Science

Department of Earth Sciences

September 2017

Title: Mass Cycling through Crustal Magma Chambers and the Influence of Thermo-Mechanical State on Magma Compositions through Time

Magma chambers are a fundamental component of crustal magma transport, modulating erupted volumes, compositions, and timing of eruptions. However, we understand little about how eruption episodicity relates to magma chamber evolution. The many influences on composition make inference of crustal processes from erupted compositions difficult, but there are patterns of eruptive evolution in well-characterized systems that suggest something systematic is occurring.

We have developed a coupled thermo-mechanical-chemical model in order to characterize melt evolution through cycles of chamber filling, rupture, and drainage in a thermally evolving, viscoelastic crust. We consider a deeply seated oblate spheroidal chamber, calculating pressure, temperature, volume, elemental concentration, partitioning between crystals and melt, and crustal temperature through time. We characterize the time dependence of chamber failure, thermal longevity, and melt concentrations on mechanical parameters and influx rates. These results should be important for constraining physical controls on eruption episodicity and predictions of instability at magmatic centers.

CURRICULUM VITAE

NAME OF AUTHOR: Constance Ozimek

GRADUATE AND UNDERGRADUATE SCHOOLS ATTENDED:

University of Oregon, Eugene, OR
University of Washington, Seattle, WA

DEGREES AWARDED:

Master of Science, Geological Sciences, 2017, University of Oregon
Bachelor of Science, Physics, 2014, University of Washington

AREAS OF SPECIAL INTEREST:

Geophysics
Volcanology

PROFESSIONAL EXPERIENCE:

Geology Instructor, Upward Bound Summer Academy, Umpqua Community College, 2017

Research Assistant, Department of Earth Sciences, University of Oregon, 2015-2017

Graduate Teaching Fellow, Department of Earth Sciences, University of Oregon, 2015-2017

Instructor, Mountain Trail Outdoor School, 2015

Senior Instructor, Pali Institute, 2013-2014

Research Assistant, Seismology Lab, Department of Earth and Space Sciences, University of Washington, 2012

Research Assistant, Pollack Laboratory, Department of Bioengineering, University of Washington, 2011

Research Assistant, Polar Science Center, Applied Physics Laboratory, University of Washington, 2010

GRANTS, AWARDS AND HONORS:

Graduate Teaching Fellowship, University of Oregon, 2015-2017

NASA Space Grant Scholarship, University of Washington, 2009-2013

Dean's List for Academic Excellence, University of Washington, 2009-2012

ACKNOWLEDGEMENTS

I thank Leif Karlstrom for being a constant support as my advisor and a wellspring of knowledge throughout my time at University of Oregon. His guidance and patience helped me to jump into the world of geology and this project. I couldn't have done it without him.

I gratefully acknowledge all the professors and graduate students in the Department of Earth Sciences at the University of Oregon who helped with all of my questions about geology, programming, and future plans and willingly supported my journey with enthusiasm.

I am grateful for the financial support from the University of Oregon Department of Earth Sciences and my advisor, Leif Karlstrom.

I give my heartfelt thanks to my husband for being my emotional support and for the many back massages given. Also, thanks to my office mate, Dan O'Hara for being a bouncing board for ideas and for the sense of camaraderie that we built.

For my parents, who have supported me every step of the way and who encouraged my curiosity and love of science.

TABLE OF CONTENTS

Chapter Page

LIST OF FIGURES

LIST OF TABLES

Table Page

CHAPTER I

INTRODUCTION

Previous Research

Complexity in volcanic eruption cycles is reflective of variations in the many interconnected processes happening in crustal plumbing systems and storage zones. Figures (1) and (2) represent two very different mafic volcanic systems. The Columbia River Basalt Group is a large igneous province that produced 210,000 km^3 of erupted material over a time period of around 10 Myr. Cerro Negro Volcano in Nicaragua is a much smaller system and has only produced 0.16 km^3 of erupted material over the last 150 years. Both show a variability in chemical concentrations, eruptive volumes, and repose times between eruptions, but operate on very different scales. These variations seen in the surface stratigraphy can be inferred to reflect the complexity and variability of the magmatic systems that sourced these eruptions.

Significant effort has been made to model and understand the dynamic evolution of magmatic systems and answer the above questions. Melting and transport dynamics can be critical to understanding rates of recharge, spatial distribution of chambers and volcanic vents, compositions of primitive melt, and the exchange of energy between transport and storage systems. All are important in understanding the emplacement, lifespan, and stability of a chamber. Some models predict how melt is produced in quantities large enough to be transported through the crust and erupted at the surface, exploring the interactions of subducting slabs, plumes, and volatiles within the mantle (Cervantes and Wallace,

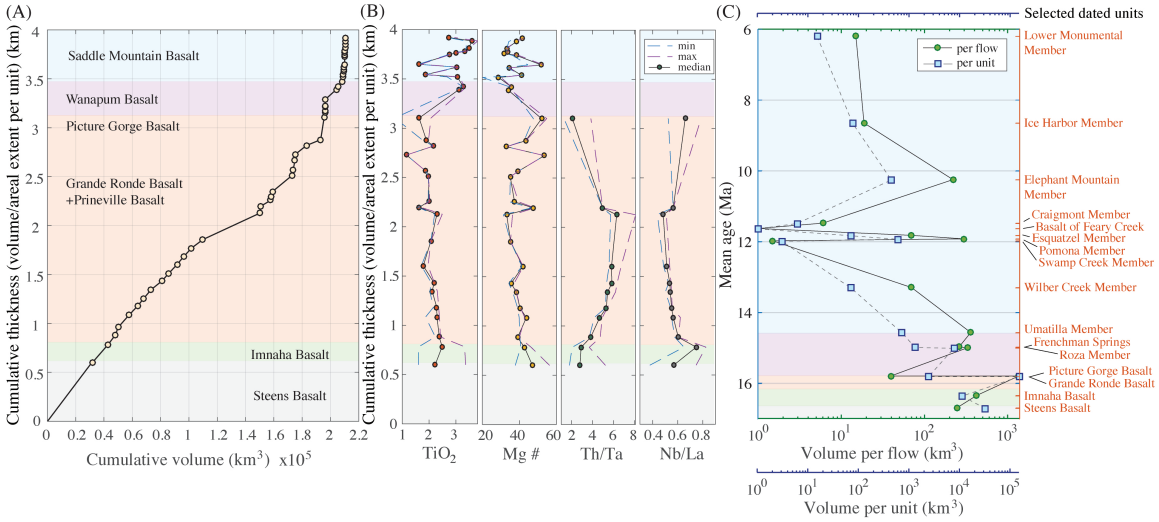

FIGURE 1. Physical and chemical stratigraphy for the Columbia River Basalt Group, a Large Igneous Province that covers parts of Washington, Oregon, and Idaho. A) Thickness is derived by dividing unit volume by areal extent (Reidel et al., 2013). B) Chemistry comes from Wolff et al. (2008) and Reidel et al. (2013). C) Volume per flow is derived by dividing unit volume by the estimated number of eruptions per unit (Reidel et al., 2013), while mean $^{40}Ar/^{39}Ar$ ages come from Barry et al. (2013).

2003; Hales et al., 2005; Bergantz, 1989; Defant and Kepezhinskas, 2001). Other models focus on the mechanics of transporting melts through crustal plumbing systems (Anderson and Segall, 2011). Some theories propose a diapiric system of emplacement for the largest and deepest chambers, their ascent driven by buoyancy (Paterson et al., 2011; Marsh, 1982), and others focus on magma ascent through individual diking events, where the connecting chambers have enough overpressure to propagate a crack tip and hold the dike open before freezing and healing of the fracture (Rivalta et al., 2005; Lister and Kerr, 1991). Stress conditions are also very important in considering transport and rupture. The free surface, tectonic background stresses, and the stress due to internal overpressures in a magma chamber can alter the direction and orientation of a propagating dike (Karlstrom et al., 2010; Gudmundsson, 2006) or cause structural failure and caldera collapse, a potential trigger for some eruptions (Gudmundsson et al., 1997; Gregg et al., 2012).

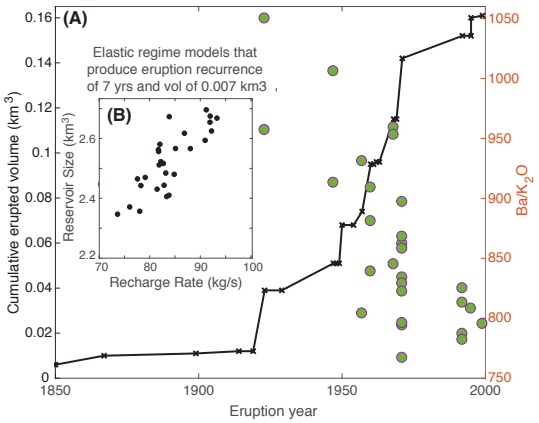

FIGURE 2. Plot of cumulative erupted volumes and years of eruptions for Cerro Negro Volcano in Nicaragua. Data is from Hill et al. (1998) and unpublished geochemical data from Terry Plank, Columbia University. We average the data from the period of increased activity in the 1900s, approximating eruption sizes of 0.007 km^3 and 7 years apart to compare with our model. B) Plot of model simulations that produce similar sized and time intervals between chamber failures. A band of recharge and initial chamber volumes that could produce such a history emerges.

Understanding the emplacement processes and growth of large, long-lived magma chambers can give insight into the path to destabilization and the controls on cyclic behavior. Annen (2009) proposed that crustal storage takes the form of stacked sills, emplaced one on top of the other. Prolonged and consistent magmatism in the crust provides a thermally primed initial geotherm that allows for the survival of long lived, mobile magmas (Karlstrom et al., 2017). Despite the difficulties presented by emplacement into cold crust without immediately freezing, shallow chambers capable of producing caldera forming eruptions can form through the conductive heating of surrounding wall rock, which allows for viscoelastic relaxation of chamber overpressures and significant growth (Degruyter and Huber, 2014; Jellinek and DePaolo, 2003; Dragoni and Magnanensi, 1989). Many mechanisms have been proposed for the destabilization of these large chambers, including increased mass injection (Jellinek and DePaolo, 2003), first

boiling and second boiling of volatiles (Blake, 1984; Fowler and Spera, 2008, 2010), and buoyancy (Caricchi et al., 2014).

The evolution of trace and major element concentrations in a chamber is sensitive to the concentrations and rates of recharge, evacuation, assimilation, and fractional crystallization (DePaolo, 1981; Spera and Bohrson, 2004; Lee et al., 2013). Mineral assemblages, distribution of stable isotopes, and fluid melt inclusions act as geothermometers and geobarometers and can be indicative of the equilibrium conditions before eruption (Ghiorso and Sack, 1991; Johnson and Rutherford, 1989). Measurement of radioactive decay and relative abundances of isotopes can represent the temporal history of magma chamber (Sigmarsson, 1996). Analysis of eruptive packages at magmatic centers uncover trace element trends indicating different melt sources and rates of recharge, levels of crustal contamination, rates crystallization, and mixing of one or more unique magmas (Yu et al., 2015; Wallace, 2004; Dungan and Rhodes, 1978). Combined, this geochemical data unveils valuable information about depths and conditions of magma storage and triggers that lead to eruption, as well as the timescales of storage versus ascent through the crust (Rubin et al., 2017). Models such as MELTS look at phase equilibria for the liquid phase and track major element response to steps in temperature and pressure (Ghiorso and Sack, 1995; Asimow and Ghiorso, 1998). Simpler bulk partition coefficient box models (Lee et al., 2013) track compositional time evolution through mass balance.

Project Overview

The magmatic plumbing system can be described as a series of steps, starting at the point of magma generation in the mantle. Magma is then transported through channels, dikes and, diapirs into the crust, where storage can occur.

Magmas either freeze and crystallize or continue their journey as the storage chamber destabilizes, ejecting magma into the crust, subsequent chambers, or to the surface. The end of only one branch of the plumbing system, volcanic eruptions that make it to the surface represent only a small fraction of the melt produced at depth. The geophysical constraints on the lower steps of the system are not well understood and model results are highly non-unique, so multifaceted datasets collected at the surface are vital in improving our understanding of the interconnected parts of the magmatic plumbing system. Research has a tendency to focus on magma chambers because they often represent the most important transport element step in the overall system. Chambers act as capacitors, holding magmas for variable periods of time and allowing complexity to generate in the system through evolving compositional, thermal, and mechanical states. As such, magma chambers are important in understanding the trends and patterns seen at volcanic centers and can give insight into some of the integral questions in the volcanology field. What controls and influences the growth and stability of a magma chamber over its lifetime? How can we predict future instabilities? How is composition of erupted lavas related to the mechanics of transport?

Modeling has now advanced to the stage where it is possible to develop self-consistent, predictive models that consider the fundamentally coupled nature of magmatic processes. We develop a thermo-mechanically and chemically coupled chamber to predict the evolution of mafic magmatic centers. By taking into account the coupled nature of physical attributes, we produce self-consistent model output which may be compared to surface data, with the future goal of providing tighter constraints on magmatic processes at depth and making more accurate predictions of instabilities within a system. Anderson and Segall (2011) point out the utility of combining physics based models that link magmatic processes

directly to observable data. The time evolution of physical and chemical processes are often highly nonlinear and need comparison to multiple data sets to constrain the parameters.

Our model consists of a thermo-mechanical box model coupled to a chemical box model. We track changes in chamber pressure, temperature, volume, densities and volume fractions of melt and crystals, and temperature profiles in the crust for each simulation (Degruyter and Huber, 2014). The thermo-mechanical model does not consider volatiles, an assumption that restricts the applicability of this model to deep, mafic chambers for which volatiles are dissolved and have limited impact on the mechanical behavior of the system. Transport to and from the chamber is also not considered, so we do not model eruptions that make it to the surface. Rather, these are chamber destabilization events that are a proxy for eruptions or intrusion to higher levels of the crust.

The chemical model is modified from Lee et al. (2013) and DePaolo (1981) and uses the thermo-mechanically informed rates and temperatures to track the changing concentrations of an element with a specified partition coefficient, D, which describes the equilibrium ratios of the element in the solid and liquid phases. The processes of interest in the chemical model are recharge, evacuation, assimilation, and fractional crystallization.

We find distinct thermo-mechanical regimes of chamber mechanical evolution through time: (1) an elastic regime characterized by a continuous cycle of chamber destabilization events, and (2) a viscous regime, which is characterized by efficient relaxation of overpressure, which yields no chamber failures and promotes chamber growth. The longevity of chambers depends on the initial volume of the chamber, influx rates, and the thermal state of the surrounding crust. We do not address the problem of magma chamber formation here.

Chemical evolution of the melt corroborates the findings of Lee et al. (2013), but within a self-consistent thermo-mechanical framework. Concentrations reach a quasi steady state, producing changes less than 5e-12 units of concentration per second, in a recharging, assimilating, erupting, and fractionally crystallizing system. Mathematically, steady state is defined when the time derivative, $\frac{dC_m}{dt}$, equals zero. However, we define a threshold within which we consider the concentration to be at steady state because the continuously changing rates of evacuation, assimilation, and crystallization prevent a mathematical steady state from being reached. Compatible elements, elements with an affinity for the crystal phase, reach steady state more quickly than incompatible elements. However, concentrations and steady state compositions are sensitive to changes in crystallization, assimilation, evacuation, and recharge, which happens, for example, when the chamber transitions from an elastic to viscoelastic regime, or when the crust heats and decreases conductive heat loss efficiency. The mechanical regime of the chamber thus is reflected in chemical composition.

Observable data, such as the timescales between eruptions, erupted volumes, and trace element concentrations, seen in Figures (1) and (2), can be compared to model output. Inset B in Figure (2) demonstrates the model's ability to predict the range of recharge rates and reservoir sizes that could produce an eruption cycle matching the average rates and erupted volumes seen at Cerro Negro Volcano. Adding further data for the model to match, such as the evolution of chemical composition, will narrow the possible ranges of input parameters further and give us a better understanding for the controls on magmatic cyclicality.

CHAPTER II

METHODS

Model Description

A system of four equations, derived from the conservation of momentum, mass, energy, and concentration, is solved, yielding the differential equations for chamber pressure, temperature, volume, and concentration. These equations in conjunction with the diffusion equation for nodes spanning from the chamber edge to the surface are solved numerically with a Matlab ODE (ordinary differential equation) solver to acquire a temporal history of chamber characteristics. The diffusion equation is semi-discretized with finite differences in the spatial domain so as to be solved alongside the other odes. Mass transfers within the system through a constant recharge rate, partitioning between crystal and melt phases, and evacuation during chamber failures. Other major processes include conductive cooling at the chamber boundary, corrected to the first order for chamber geometry, and viscous relaxation as the crust heats and decreases in viscosity. The graph on the right of Figure (3) shows a sample crustal temperature profile plotted with depth.

It should be noted that the thermo-mechanical model functions on the assumption that crystals and melt are homogeneous within the chamber, whereas the chemical model assumes instantaneous removal of the crystals in order to advance melt composition. We do not consider any intra-chamber dynamics or zoning, assuming instantaneous mixing in the thermo-mechanical model and instantaneous settling for the chemical model. Volatiles are taken out of consideration for simplification. Physically this could correlate with a system that has gone through crustal degassing and is in a later stage of the eruptive

cycle (Sibik et al., 2015) or a deep system with high lithostatic pressures that makes exsolution inconsequential within the chamber. Major assumptions and simplifications were made for this project, however, it is nonetheless an improvement over existing models. The future of this project will address some of the oversimplifications and work towards resolving discrepancies between the two box models.

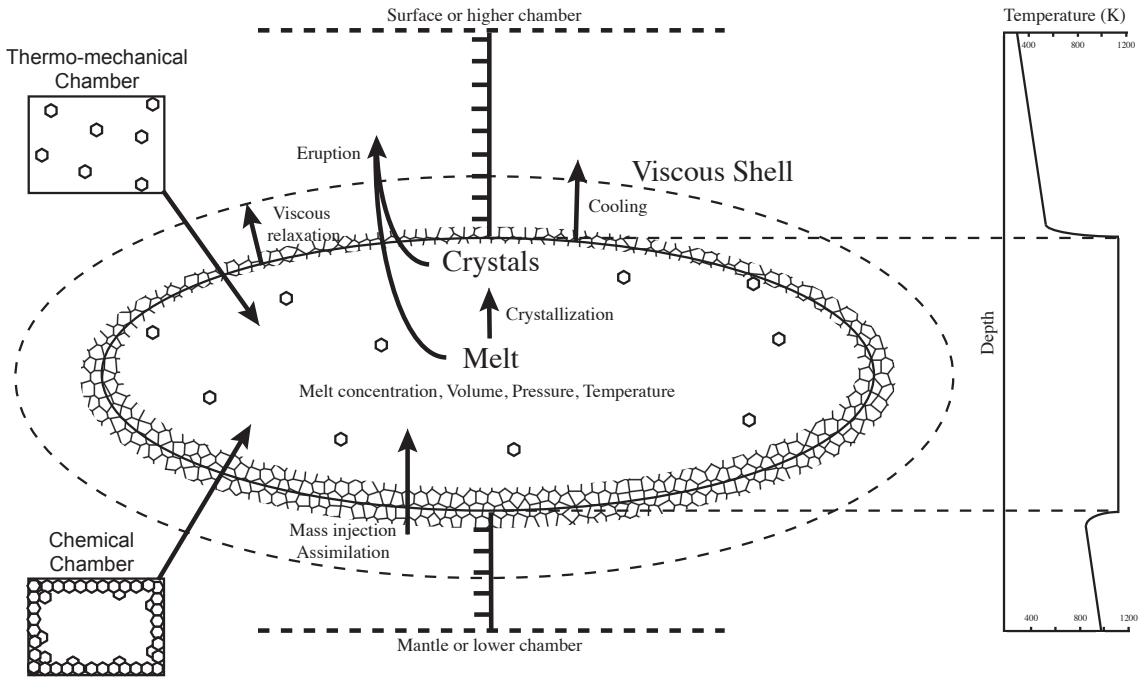

FIGURE 3. A simple representation of the thermo-mechanical-chemical box model. Important processes that the model considers are magma recharge, evacuation through chamber failure, crystallization of the melt, and assimilation of crustal components. The thermal-mechanical model considers crystals to be homogeneous within the melt, whereas the chemical model assumes crystals are removed from the melt. Evolution of chamber pressure, temperature, volume, and concentration are solved for. A representative crustal temperature profile is shown to the right. Crustal temperature evolution is solved for in one-dimension.

Conservation of Momentum

We consider a Maxwell visco-elastic rheology for crustal rocks surrounding the chamber (Degruyter and Huber, 2014; Dragoni and Magnanensi, 1989; Jellinek

TABLE 1. Symbol definitions.

Symbol	Definition	Units
a_1	coefficient for crustal strength functions	
b_1	coefficient for crustal strength functions	
b	power law exponent	
c	complex distance to spheroid focii	
c_p	specific heat capacity	$\mathrm{Jkg^{-1}K^{-1}}$
k	thermal conductivity of crust	$\mathrm{Js^{-1}m^{-1}K^{-1}}$
m_m	mass of element in melt	kg
$\dot{m}_m^{in}$	element mass influx rate	$\mathrm{kgs^{-1}}$
$\dot{m}_m^{out}$	element mass outflux rate	$\mathrm{kgs^{-1}}$
t	time	s
A	material dependent constant for viscosity calculation	Pas
B	molar gas constant	$\mathrm{Jmol^{-1}K^{-1}}$
C_{in}	recharge concentration	
C_m	melt concentration	
C_{WR}	crust concentration	
D	partition coefficient	
De	Deborah number	
G	activation energy for creep	$\mathrm{Jmol^{-1}}$
H	total enthalpy	$\mathrm{Js^{-1}}$
$\dot{H}_{in}$	enthalpy inflow rate	$\mathrm{Js^{-1}}$
$\dot{H}_{out}$	enthalpy outflow rate	$\mathrm{Js^{-1}}$
$\dot{H}_{cool}$	cooling enthalpy outflow rate	$\mathrm{Js^{-1}}$
L_m	latent heat melting	$\mathrm{Jkg^{-1}}$
M	total mass	kg
M_x	crystal mass	kg
$\dot{M}_A$	assimilation rate	$\mathrm{kgs^{-1}}$
$\dot{M}_{in}$	recharge rate	$\mathrm{kgs^{-1}}$
$\dot{M}_{out}$	eruption rate	$\mathrm{kgs^{-1}}$
$\dot{M}_x$	crystallization rate	$\mathrm{kgs^{-1}}$
N	number of eruptions before mechanically locked	
P	chamber pressure	Pa
P_{lith}	lithostatic pressure	Pa
ΔP	chamber overpressure above lithostatic pressure	Pa
ΔP_{crit}	critical overpressure	Pa
r_a	semi-minor axis length	m
r_b	semi-major axis length	m
T	chamber temperature	K
T_L	liquidus temperature	K
T_S	solidus temperature	K
Tr	transport number	
V	chamber volume	$\mathrm{m^3}$
α_m	melt thermal expansion coefficient	$\mathrm{K^{-1}}$
α_x	crystal thermal expansion coefficient	$\mathrm{K^{-1}}$
α_r	crust thermal expansion coefficient	$\mathrm{K^{-1}}$
β_e	effective compressibility	Pa
β_m	melt bulk modulus	Pa
β_x	crystal bulk modulus	Pa
β_r	crust bulk modulus	Pa
ϵ_m	melt volume fraction	
ϵ_x	crystal volume fraction	
η_r	viscosity of the crust	Pa s
μ	crust shear modulus	Pa
ν	crust Poisson's ratio	
$\bar{\Theta}(z)$	averaged crustal shell temperature	K
κ	thermal diffusivity of crust	$\mathrm{m^2s^{-1}}$
ρ	mixture density	$\mathrm{kgm^{-3}}$
ρ_m	melt density	$\mathrm{kgm^{-3}}$
ρ_x	crystal density	$\mathrm{kgm^{-3}}$
τ_{in}	injection timescale	s
τ_{cool}	cooling timescale	s
τ_{relax}	viscous relaxation timescale	s

and DePaolo, 2003) that has purely volumetric strain. The volume of the chamber fluctuates with pressure changes caused by recharge, evacuation, crystallization, and viscous relaxation in the crust. Chamber failures are triggered when the overpressure, the difference between total magma and lithostatic pressure, reaches a critical threshold and are subsequently terminated when the pressure hits lithostatic again. A critical overpressure value is set because rock has a finite strength and cannot support overpressure that produces stresses exceeding this strength. Things that may influence the critical value include heterogeneities in the crust, anisotropies, tensile strength of the surrounding rock, distance to the free surface, and concentration of stresses through chamber geometry (Gudmundsson, 2012). Variables used in the equation are chamber volume V, bulk compressibility β_r, chamber pressure P, lithostatic pressure P_{lith}, and effective viscosity η_r.
The elastic response of the oblate spheroidal chamber is considered in full space (Cervelli, 2013). Most models consider spherical chambers. We generalize to an oblate spheroidal chamber, which is an improvement on current thermo-mechanical models towards a more realistic chamber geometry. The constrained crustal properties and volumetric response to stress allow for realistic chamber boundary expansion and contraction rates. These realistic rates are necessary for stabilizing the finite difference scheme used to solve for the temperature in the crust.

Equations for the elastic response to chamber pressurization come from Cervelli (2013). The semi-minor and semi-major axes of the oblate spheroid are r_a and r_b respectively and c is the distance to the focal points. θ, a_1, and b_1 are constants defined using the axes specifications and crustal properties, μ the shear modulus and ν Poisson's ratio of the crust.

$$c = \sqrt{r_a^2 - r_b^2} \tag{2.1}$$

$$\theta = \text{ArcTan}[r_a^2 - c^2, -2r_a c] \tag{2.2}$$

$$a_1 = \frac{-2r_b^2(r_a^2 + 2r_b^2)c - 3r_a r_b^4\theta}{4r_a c^2(-r_b^2 + r_a^2(-1+\nu)) + 2r_b^2 c(r_b^2 + 2r_a^2(-1+\nu))\theta + r_a r_b^4(1+\nu)\theta^2} \tag{2.3}$$

$$b_1 = \frac{4r_a^2 c(-1+\nu) + 2r_b^2 c(-3+2\nu) + r_a r_b^2(-5+4\nu)\theta}{4r_a c^2(-r_b^2 + r_a^2(-1+\nu)) + 2r_b^2 c(r_b^2 + 2r_a^2(-1+\nu))\theta + r_a r_b^4(1+\nu)\theta^2} \tag{2.4}$$

The Maxwell viscoelastic crustal response to chamber pressurization and the thermal expansion response to changes in temperature within the melt are accounted for in the conservation of momentum. Viscosity, η, decreases with time as the crust warms. It is calculated using an Arrhenius law (Jellinek and DePaolo, 2003; Karlstrom et al., 2010), where G is the activation energy for viscous creep, B is the molar gas constant, and $\bar{\Theta}(z)$ is the averaged temperature in the shell of crust from the chamber boundary to a specified radius, shown by

$$\eta = A\text{exp}\Big(\frac{G}{B\bar{\Theta}(z)}\Big). \tag{2.5}$$

An effective compressibility, β_e can be defined as

$$\beta_e = \frac{1}{V}\Big[\frac{2b^2\pi}{3\mu}(a_1(alog(\frac{a-c}{a+c})(-1+2\nu) + c(-5+4\nu)) - 2c^3 b_1)\Big], \tag{2.6}$$

yielding a canonical form for the conservation of momentum equation as follows:

$$\frac{1}{V}\frac{dV}{dt} = \frac{1}{\beta_e}\frac{dP}{dt} + \frac{P - P_{lith}}{\eta} - \alpha_r\frac{dT}{dt}. \tag{2.7}$$

Conservation of Mass

A simple mass balance is used that considers the external input of mass to the chamber through recharge and output of mass through chamber failure. The momentum balance controls the timing of chamber failures and initiates the start and stop of mass outflux. The most general form of the conservation of mass equation is

$$\frac{dM}{dt} = \dot{M}_{in} - \dot{M}_{out}. \tag{2.8}$$

The time derivative of mass is dependent on the changing volume, V, and magma density, ρ.

$$\frac{\dot{M}_{in} - \dot{M}_{out}}{\rho V} = \frac{1}{\rho}\frac{d\rho}{dt} + \frac{1}{V}\frac{dV}{dt} \tag{2.9}$$

The volume fractions of melt and crystals, ϵ_m and ϵ_x, add up to one at all times. Mixture density is calculated by adding the multiplied volume fractions and respective densities. Equations of state for melt and crystal densities are dependent on the compressibility, β_m and β_x, thermal expansion coefficients, α_m and α_x, and rates of pressure and temperature change.

$$\epsilon_m + \epsilon_x = 1 \tag{2.10}$$

$$\rho = \epsilon_m \rho_m + \epsilon_x \rho_x \tag{2.11}$$

$$\frac{1}{\rho_m}\frac{d\rho_m}{dt} = \frac{1}{\beta_m}\frac{dP}{dt} - \alpha_m \frac{dT}{dt} \tag{2.12}$$

$$\frac{1}{\rho_x}\frac{d\rho_x}{dt} = \frac{1}{\beta_x}\frac{dP}{dt} - \alpha_x\frac{dT}{dt} \tag{2.13}$$

$$\frac{1}{\rho}\frac{d\rho}{dt} = \frac{1}{\rho}\left(\epsilon_m\frac{d\rho_m}{dt} + \epsilon_x\frac{d\rho_x}{dt} + (\rho_x - \rho_m)\frac{d\epsilon_x}{dt}\right) \tag{2.14}$$

Crystal volume fraction is dependent on temperature and the power law exponent, b, which approximates the magma composition. Equations for volume fraction were adapted from Huber et al. (2009) for the case of no volatiles.

$$\epsilon_x = \left(1 - \left(\frac{T - T_S}{T_L - T_S}\right)^b\right) \tag{2.15}$$

$$\frac{\partial\epsilon_x}{\partial T} = -\left(b\frac{(T - T_S)^{b-1}}{(T_L - T_S)^b}\right) \tag{2.16}$$

$$\frac{d\epsilon_x}{dt} = \frac{\partial\epsilon_x}{\partial T}\frac{dT}{dt} \tag{2.17}$$

By substituting the above equations into equation (2.8), we come to the final equation for the conservation of mass. All variables shown can be expressed in terms of pressure, temperature, chamber volume, or constants.

$$\frac{\dot{M}_{in} - \dot{M}_{out}}{V} = \left[\frac{\epsilon_m\rho_m}{\beta_m} + \frac{\epsilon_x\rho_x}{\beta_x}\right]\frac{dP}{dt} + \left[(\rho_x - \rho_m)\frac{\partial\epsilon_x}{\partial T} - \alpha_x\epsilon_x\rho_x - \alpha_m\epsilon_m\rho_m\right]\frac{dT}{dt} + \left[\frac{\rho}{V}\right]\frac{dV}{dt} \tag{2.18}$$

Conservation of Energy

The conservation of energy accounts for sensible as well as latent heat. Similar to the conservation of mass, we expand a simple equation that balances the enthalpy fluxing in and out of the chamber, as shown by

$$\frac{dH}{dt} = \dot{H}_{in} - \dot{H}_{out}. \tag{2.19}$$

Enthalpy is added to the chamber through recharge, where c_p is the specific heat capacity, T_L is the liquidus and injection temperature, and $\dot{M}_{in}$ is the rate of recharge. Enthalpy leaves the chamber through eruption and conduction into the surrounding wall rock, where T is the chamber temperature and $\dot{M}_{out}$ is the eruption rate. The spatial derivative of temperature in the crust at the chamber boundary, $\frac{\partial \Theta}{\partial z}$, is approximated with second order finite differences. δ is a geometric correction factor that estimates the increase in conduction rates for a spherical chamber from a planar geometry, which is calculated by comparing the steady state heat flux for a sphere to the heat flux from a plane (equation 2.23). The projection of the oblate spheroid onto a flat plane is used to calculate heat flux from a plane, and considers conduction above and below the plane. k is the thermal conductivity of the crust.

$$\dot{H}_{in} = c_p T_L \dot{M}_{in} \tag{2.20}$$

$$\dot{H}_{out} = c_p T \dot{M}_{out} + \dot{H}_{cool} \tag{2.21}$$

$$\dot{H}_{cool}(t) = -k\delta \frac{\partial \Theta}{\partial z} \tag{2.22}$$

$$\delta = \frac{Q_{sphere}}{Q_{plane}} \tag{2.23}$$

The enthalpy in the chamber consists of sensible heat, latent heat of crystallization, and the pressure-volume work, arising from the expansion of the chamber in response to pressurization.

$$H = \rho c T V - L_m \rho_x \epsilon_x V + P \Delta V \tag{2.24}$$

$$\frac{dH}{dt} = \rho cT\frac{dV}{dt} + \rho cV\frac{dT}{dt} + cTV\frac{d\rho}{dt} - L_m\rho_x\epsilon_x\frac{dV}{dt} - L_m\rho_x V\frac{d\epsilon_x}{dt} - L_m\epsilon_x V\frac{d\rho_x}{dt} + P\frac{dV}{dt} \quad (2.25)$$

Expanding the terms in equations (2.19) using the equations above and the identities from the conservation of mass section, the final equation for the conservation of enthalpy is then expressed as

$$\frac{\dot{H_{in}} - \dot{H_{out}}}{\rho cTV} = \left[\frac{1}{\rho}\left(\frac{\epsilon_m\rho_m}{\beta_m} + \frac{\epsilon_x\rho_x}{\beta_x}\right) - \frac{L_m\epsilon_x\rho_x}{\rho cT\beta_x}\right]\frac{dP}{dt} + \left[\frac{(\rho_x - \rho_m)}{\rho}\frac{\partial\epsilon_x}{\partial T} + \frac{1}{T} - \frac{L_m\rho_x}{\rho cT}\frac{\partial\epsilon_x}{\partial T} + \frac{L_m\epsilon_x\alpha_x\rho_x}{\rho cT} - \frac{\epsilon_m\rho_m\alpha_m}{\rho} - \frac{\epsilon_x\rho_x\alpha_x}{\rho}\right]\frac{dT}{dt} + \left[\frac{1}{V} - \frac{L_m\rho_x\epsilon_x}{\rho cTV} + \frac{P}{\rho cTV}\right]\frac{dV}{dt}. \quad (2.26)$$

Important Assumptions

We view the magma chamber as an element embedded into a larger system. What occurs inside and outside the chamber are fundamentally different problems and as such, we must make assumptions about the rest of the system in order to focus on the chamber scale. We assume that the chamber is deep seated or has gone through significant degassing prior to consideration in order to justify the neglect of volatiles. The chamber is defined as an oblate spheroid with fixed aspect ratio in full space. The crust is considered to be a Maxwell viscoelastic material that has averaged material properties and constant stress. The thermo-dynamic model defines the magma chamber as an instantaneously homogeneous black box that does not account for mixing, zonation, or thermal gradation within the chamber. The chemical model defines the chamber with the assumption that crystals instantaneously settle out of melt through fractional crystallization, storing melt and crystals in separate reservoirs. This allows for the evolution of bulk melt composition, as it would not evolve with crystallization if melt and crystal phases were held in equilibrium. Phase equilibria are assumed constant throughout the lifetime of the chamber to justify a constant elemental partition coefficient, constant exponent value b through time in the melt fraction-temperature

parameterization, and constant latent heats. We assume a mafic system because mafic magmas have simpler phase diagrams. The diffusion of heat through the crust is solved for in one dimension, however, a simple and constant correction factor is used to link to chamber geometry. We consider a time variant boundary condition to consistently take into account chamber expansion. In order to solve the heat equation over a variable domain, we transform onto a fixed domain. This numerically adds an advection term into the diffusive heat equation.

Significant assumptions were made in order to derive a numerically tractable and efficient model. However, this model is still an improvement on current magma chamber models because it considers the mechanical affects on compositional evolution, includes a more realistic chamber geometry, and solves for crustal temperature in a variable domain. This is meant to be a simple stepping stone along the path to link together the highly complex and fundamentally coupled processes that influence a chamber. It is possible to consider further embedded models into the framework of the chamber, looking at things such as mixing and thermal gradation, however, that is beyond the scope of this project. Similarly, one could envision embedding this chamber model, perhaps coupled mechanically to higher or lower magma chambers, in a large-scale tectonic-magmatic model of the crust or to an integrated volcanic systems model that includes conduit flow and plume processes in the atmosphere.

Conservation of Element Concentration

Our goal in this model is to move towards combining the wealth of igneous petrology knowledge with physics based chamber dynamics. This gives us insight into the influence of chamber dynamics on composition. In order to fully link the two sides of the model, we would need to consider the phase equilibria, their evolution throughout time, and their influence on thermo-dynamic response. This would require the use of thermodynamic phase equilibria models, such as MELTS, that would be continuously called for each pressure and temperature step. This is much too complicated for the scope

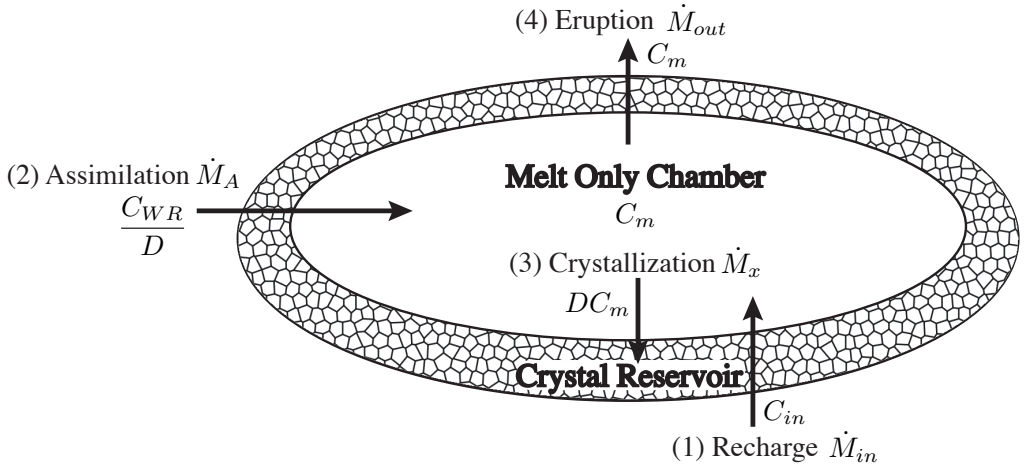

FIGURE 4. Chemical Box Model. Melt and crystals are assumed to be in separate reservoirs with an instantaneously settling assumption. The main processes controlling compositional evolution of a single element with partition coefficient D are recharge, evacuation, fractional crystallization, and assimilation.

of this project, so we consider a single element with a fixed partition coefficient reflective of an overall mafic composition.

To expand and solve for the changing concentration of an element in the melt, we start with a mass balance for a single element in the melt. Mass of the element is increased in the chamber through recharge and assimilation (processes (1) and (2) in Figure 4) and decreased through eruption and crystallization (processes (3) and (4)). A fractional crystallization scheme with instantaneous settling is considered to evolve the melt composition. The change in element mass in the chamber follows in the equation below, with m_m denoting the mass of the element in the melt. C_{in}, C_{WR} and C_m are the concentrations of the element in the injected magma, wall rock, and chamber melt respectively and $\dot{M}_{in}$, $\dot{M}_A$, $\dot{M}_x$, and $\dot{M}_{out}$ are the mass injection, assimilation, crystallization, and eruption rates. The partition coefficient, D, is defined by the ratio of an element between the melt and crystal phases, influenced by pressure, temperature, and overall melt compositions. Incompatible elements, such as zirconium and hafnium in basaltic magmas, have a partition coefficient of less than one and become enriched in a crystallizing magma, whereas compatible elements, such as nickel and cobalt in basaltic magmas, have a partition coefficient greater than one and become depleted.

When the partition coefficient is multiplied with the concentration of the magma, it yields the fraction of crystallized mass that is composed of the element and inversely, the concentration of the element in the surrounding wall rock divided by the partition coefficient yields the fraction of assimilated mass that is composed of the element.

$$\frac{dm_m}{dt} = \dot{m}_m^{in} - \dot{m}_m^{out} \tag{2.27}$$

$$m_m = C_m \rho_m \epsilon_m V \tag{2.28}$$

$$\frac{dm_m}{dt} = C_m \rho_m \epsilon_m \frac{dV}{dt} + C_m \rho_m V \frac{d\epsilon_m}{dt} + C_m \epsilon_m V \frac{d\rho_m}{dt} + \rho_m \epsilon_m V \frac{dC_m}{dt} \tag{2.29}$$

$$\dot{m}_m^{in} - \dot{m}_m^{out} = C_{in}\dot{M}_{in} + \frac{C_{WR}}{D}\dot{M}_A - DC_m\dot{M}_x - C_m\dot{M}_{out} \tag{2.30}$$

The mass of crystals and crystallization rate are defined as

$$M_x = \epsilon_x \rho_x V \tag{2.31}$$

and

$$\dot{M}_x = \rho_x V \frac{d\epsilon_x}{dt} + \rho_x \epsilon_x \frac{dV}{dt} + \epsilon_x V \frac{d\rho_x}{dt}. \tag{2.32}$$

Expanding equation (2.27) to incorporate previous identities and equations, expressing everything in terms of pressure, temperature, chamber volume, concentration, and constants yields the canonical equation

$$\frac{C_{in}\dot{M}_{in} + \frac{C_{WR}}{D}\dot{M}_A - C_m\dot{M}_{out}}{C_m \epsilon_m \rho_m V} = \left[\frac{1}{\beta_m} + \frac{D\epsilon_x\rho_x}{\beta_x \epsilon_m \rho_m}\right]\frac{dP}{dt} + \Bigg[- \alpha_m - \frac{1}{\epsilon_m}\frac{\partial \epsilon_x}{\partial T} - \frac{D\epsilon_x\rho_x\alpha_x}{\epsilon_m\rho_m}$$

$$+ \frac{D\rho_x}{\epsilon_m\rho_m}\frac{\partial\epsilon_x}{\partial T}\Bigg]\frac{dT}{dt} + \left[\frac{1}{V} + \frac{D\epsilon_x\rho_x}{\epsilon_m\rho_m V}\right]\frac{dV}{dt} + \left[\frac{1}{C_m}\right]\frac{dC_m}{dt}. \tag{2.33}$$

CHAPTER III

RESULTS

Thermo-Mechanical Results

To run a simulation, parameters such as chamber depth, recharge rates, chamber semi-minor axis length, partition coefficient, and wallrock concentrations are specified. The ODE solver then steps through time while ensuring stability of the pressure, volume, temperature, and concentration solutions. If overpressure, the difference between total magma pressure and lithostatic pressure, reaches the critical threshold, a chamber failure is triggered and evacuation rates are turned on. Simulations run until the chamber becomes mechanically locked, which we consider to be at a crystal volume fraction of 0.5, or until a specified time.

Three eruptive regimes emerge in the thermo-mechanical plots, as seen in Figure (5). The first regime is an elastic regime that builds overpressure quickly such that the chamber fails frequently. This is characterized by small chamber volumes and large influx rates. The second regime is a viscoelastic regime that relaxes overpressure back to the background lithostatic pressure such that the chamber remains stable until freezing. This is characterized by large initial chamber volumes and smaller influx rates. The third regime transitions between the elastic and viscoelastic regimes, crossing the threshold where chamber failures turn off. The time to this transition is characterized by a cooling timescale and is dependent on the efficiency with which a chamber can heat up the surrounding crust.

Characteristic timescales of the governing equations dictate dynamic behavior of equations

Varying input values results in different behaviors and regimes emerging from our model, stemming from key processes acting over different timescales (Figures 5 and

6). The timescales emerge from non-dimensional analysis of the governing equations, distilling the major controls on chamber behavior. Considered in our analysis of the model are the injection timescale, τ_{in}, cooling timescale, τ_{cool}, and viscous relaxation timescale, τ_{relax}, defined in equations (3.1-3.3). The injection timescale is the time it takes for integrated recharge mass to equal the initial chamber mass and is defined using initial melt density, ρ_0, initial chamber volume, V_0, and recharge rate, $\dot{M}_{in}$. The cooling timescale is the time it takes for heat to conduct to a characteristic length, defined using the semi-minor axis of the oblate spheroid, r_a, and thermal diffusivity, κ. The relaxation time is the time it takes for the crust to relax the critical overpressure back to lithostatic pressure and is defined using a fixed reference viscosity, η_r, and the critical overpressure, ΔP_{crit}.

Dimensionless numbers come from the idea that physical laws can be expressed using only a specified number of dimensionless ratios or products. If chosen correctly, they uniquely describe characteristic behaviors of the system, which is helpful in identifying the main components influencing chamber behavior in this model. We define the dimensionless transport number, **Tr**, as the ratio between cooling and injection timescales and the dimensionless Deborah number, **De**, as the ratio between relaxation and injection timescales, shown in equations (3.4) and (3.5), to describe our model results.

The tranport number looks at the processes controlling heat supplied through recharge and heat lost through conduction into the crust. This influences whether or not a chamber will fail before freezing. When chambers are large and recharge rates low, the transport number is small. This means that heat is lost faster through conduction than it can be supplied through recharge. This is characterized by rapid crystallization and fewer chamber failures. When chambers are small and recharge rates large, the transport number is also large. This indicates that heat is supplied quickly and this rapid injection can trigger chamber failure.

The Deborah number is a comparison of pressurization to viscous relaxation processes of the surrounding crust. When mass recharge rates are large and chamber size small, the Deborah number is greater than one. This indicates that the crust cannot relax away overpressure on the timescales considered, and therefore will respond elastically to pressure changes. When recharge rates are small and chamber size large, the Deborah number is less than one. This indicates that the timescales considered are long enough for overpressure to be relaxed away and for the crust to behave viscously.

The transition to a stable, viscoelastic regime is well represented by the Deborah number. In Figure (6), the black dotted line equals a Deborah number of one, below which the chamber simulations reach the viscoelastic transition before freezing. Above the transition line, the chambers freeze while still in the unstable elastic regime. Fixed values are used to define the dimensionless numbers, so some non-conformity occurs near the boundary of our predicted viscoelastic transition.

$$\tau_{in} = \frac{\rho_0 V_0}{\dot{M}_{in}} \tag{3.1}$$

$$\tau_{cool} = \frac{r_a^2}{\kappa} \tag{3.2}$$

$$\tau_{relax} = \frac{\eta_r}{\Delta P_{crit}} \tag{3.3}$$

$$\mathrm{Tr} = \frac{\tau_{cool}}{\tau_{in}} \tag{3.4}$$

$$\mathrm{De} = \frac{\tau_{relax}}{\tau_{in}} \tag{3.5}$$

Role of background temperature gradient

Background geotherms can have a large affect on the thermo-mechanical behavior of a chamber. This is most often changed with depth, however, it can be overwhelmed in cases with prior crustal magmatism. The lower the emplacement depth, the higher the initial temperatures, making it much easier for a chamber to start in or transition to the viscoelastic regime. This phenomena can also be recreated by adjusting the initial conditions of emplacement. If an area in the crust has been subject to long term magmatism, the crustal temperature profile will be hotter than the expected geotherm. Figure (7) explores this idea by running three simulations with identical input except for the geotherm the chamber is emplaced into. Assuming constant magma flux rates into the crust at 1e-3 km^3/yr, the three geotherms follow the heating evolution within the crust from an initial time before magmatism to a hundred thousand years after the onset of magmatism (Karlstrom et al., 2017). When emplaced into the cold crust, the chamber behaves elastically and produces several chamber failures, whereas when emplaced in the heated crust, overpressure is relaxed long before a chamber failure can occur.

This is also exhibited in Figure (6). Chambers initially in the elastic regime, characterized by blue, green, and red colors, display a downward progression towards the viscoelastic transition line as the initial geotherm is heated. The viscosity in the shell starts at a lower value, making the chambers more prone to cross the viscoelastic transition before freezing. As the initial geotherm is heated, the zone producing one through fourteen eruptions (blue and green colors) is also compressed. This is because the heated crust behaves like an insulator, slowing the rate of conduction into the surrounding wall rock and increasing the cooling timescale. This results in chambers surviving longer before freezing and a reduction of efficiency with which viscosity is lowered. This allows more chamber failures to occur before the chamber freezes or reaches the viscoelastic transition, given that it started in the elastic regime. This results in a compressed region of small to medium numbers of chamber failures and an enlarged region of higher numbers of chamber failures with increasing geotherm temperatures.

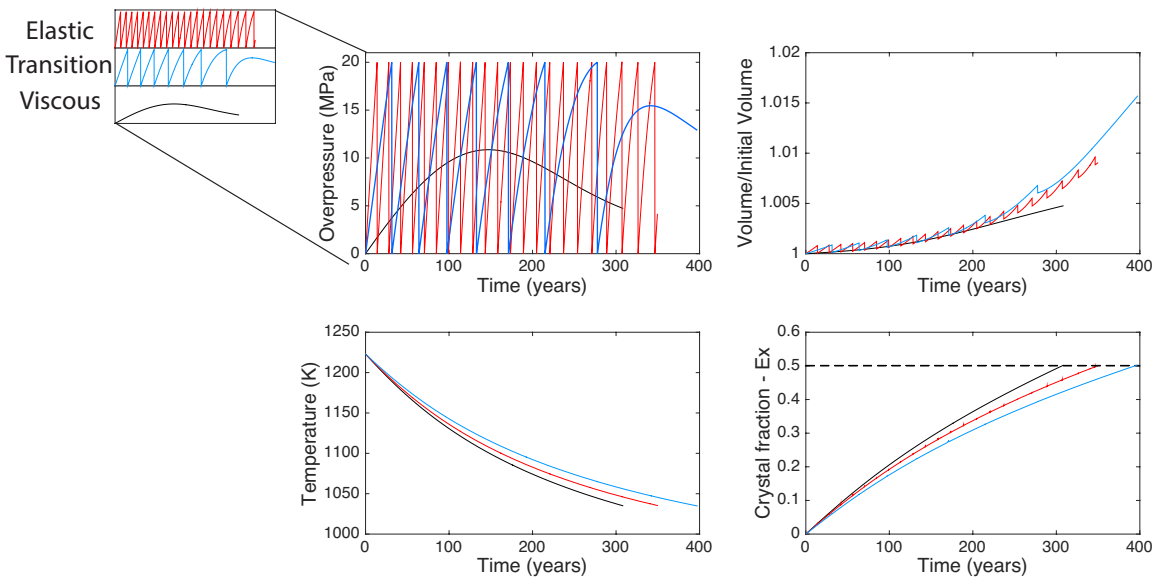

FIGURE 5. Thermo-mechanical plots for three model runs. The three chamber regimes are shown: (Red) demonstrates an elastic regime where overpressure builds quickly and chamber failure occurs frequently when a threshold overpressure is achieved, (Blue) represents the transition from an initially elastic into a viscoelastic regime, relaxing overpressure faster than it can build, and (Black) shows a stable chamber that never builds enough pressure to fail.

Time variation in period between chamber failure events

An increasing time between chamber failures as the chamber approaches the viscoelastic transition is another interesting thermo-mechanical phenomena that has emerged, as shown in Figure (8). As the surrounding crust heats up and begins to relax overpressure, it takes more time to reach the critical chamber failure threshold. In our model, we see times between chamber failures increasing as the Deborah number approaches one. This may have large implications for interpreting sequences of eruptions at volcanic centers (Figure 2). The recurrence interval may be misleading in approximating when future eruptions will occur if the chamber is approaching a Deborah number of one and the viscoelastic transition (Anderson and Segall, 2011; Segall, 2016). The model considers constant rates throughout the simulation, which is not necessarily representative of natural systems. Time-sequences of eruptions at volcanic centers are complicated by variations in recharge rates, crustal strength, and viscosities, as well as

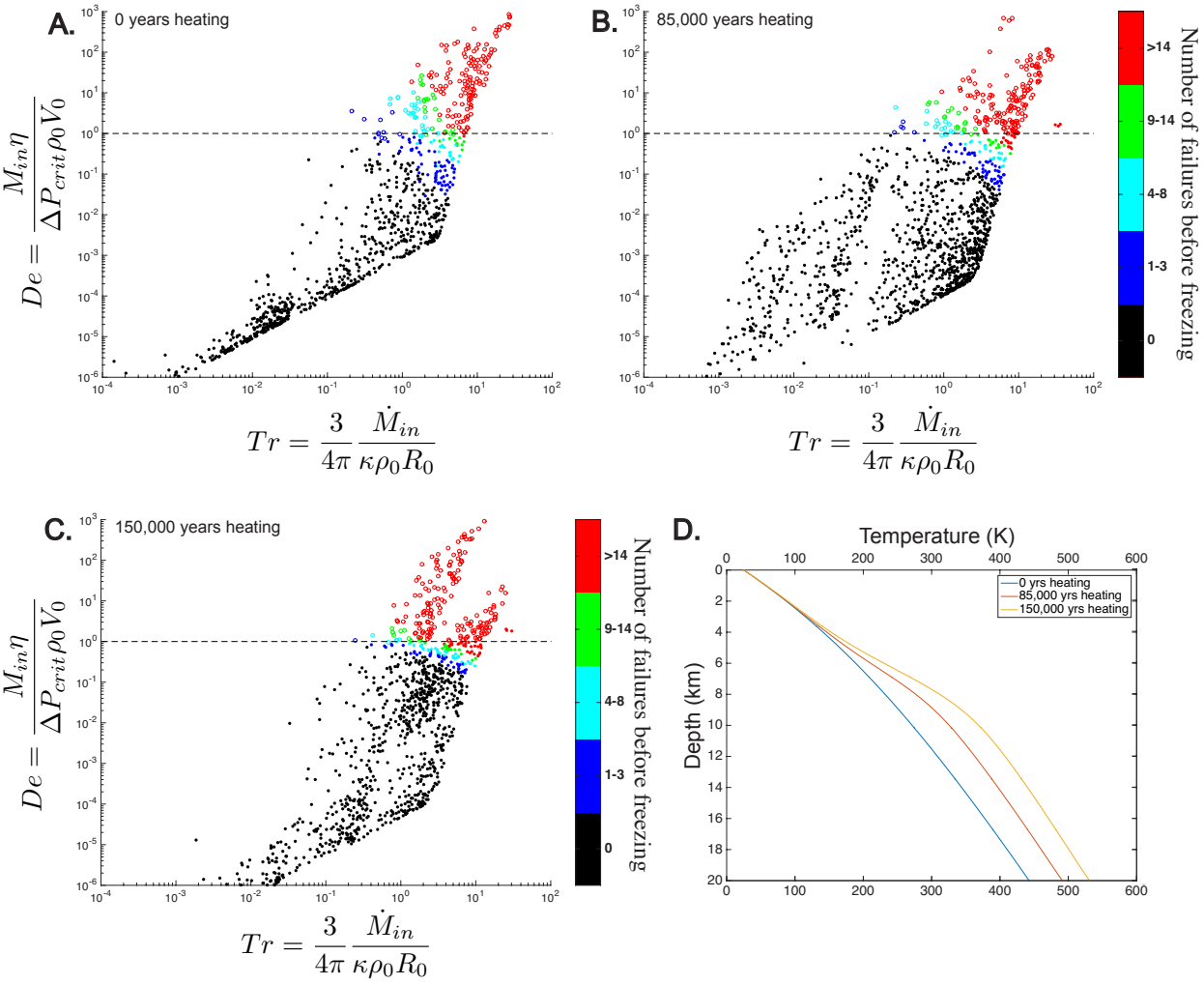

FIGURE 6. Viscoelastic transitions and number of chamber failures for three initial geotherms. Colors indicate the number of chamber failures occurring before the chamber freezes. Filled in dots indicate that the chamber passed into the viscoelastic regime before the end of the simulation and open dots remained in the elastic regime. The dashed line indicates a Deborah number of 1, where the viscoelastic transition is predicted to happen. The three panels represent three initial geotherms, shown in panel D. The simulations are run at a depth of 15km, sampling recharge rates of 0.01-100 kgs^{-1} and initial semi-minor axis of 10-1000m. A) A geotherm with no heating due to prior magmatism, B) 85,000 years of prior heating, and C) 150,000 years of prior heating. D) Geotherms during progressive volumetric crustal heating from sequential dike emplacement, cooling and crystallizing over 10s of km (Karlstrom et al., 2017).

the pre-history of crustal stress and geotherm from prior magma transport. A detailed study comparing model output to datasets will be required to further explore this topic.

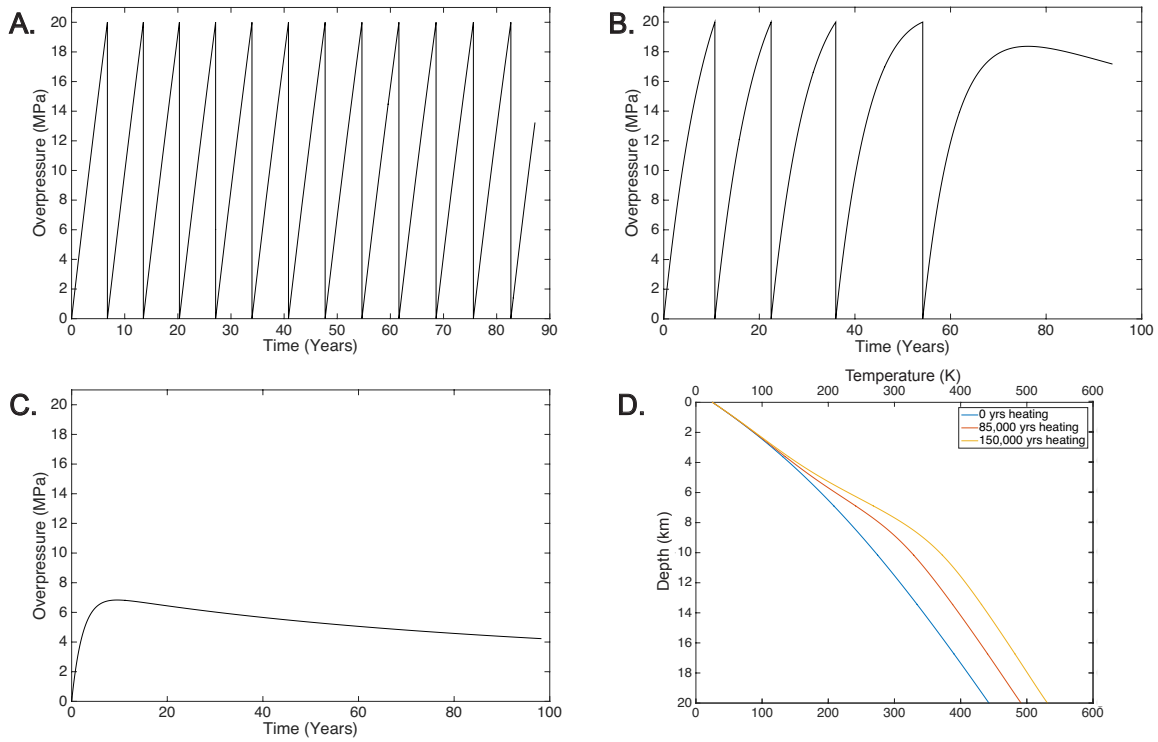

FIGURE 7. The thermo-mechanical effects of emplacing a chamber into a heated crust. Background magmatism rates into the crust are set to 1e-3 km^3/yr. Simulations were run with a recharge rate of 3 kgs^{-1}, chamber depth of 15km, and small initial volume of 0.1 km^3. A) Chamber emplaced into a cold crust, lasting 87 years until freezing; B) Chamber emplaced into a heated crust that has experienced 85,000 years of magmatism, lasting 94 years until freezing; C) Chamber emplaced into a heated crust that has experienced 150,000 years of magmatism, surviving 98 years before freezing. D) Shows geotherms used for panels, taken from Karlstrom et al. (2017).

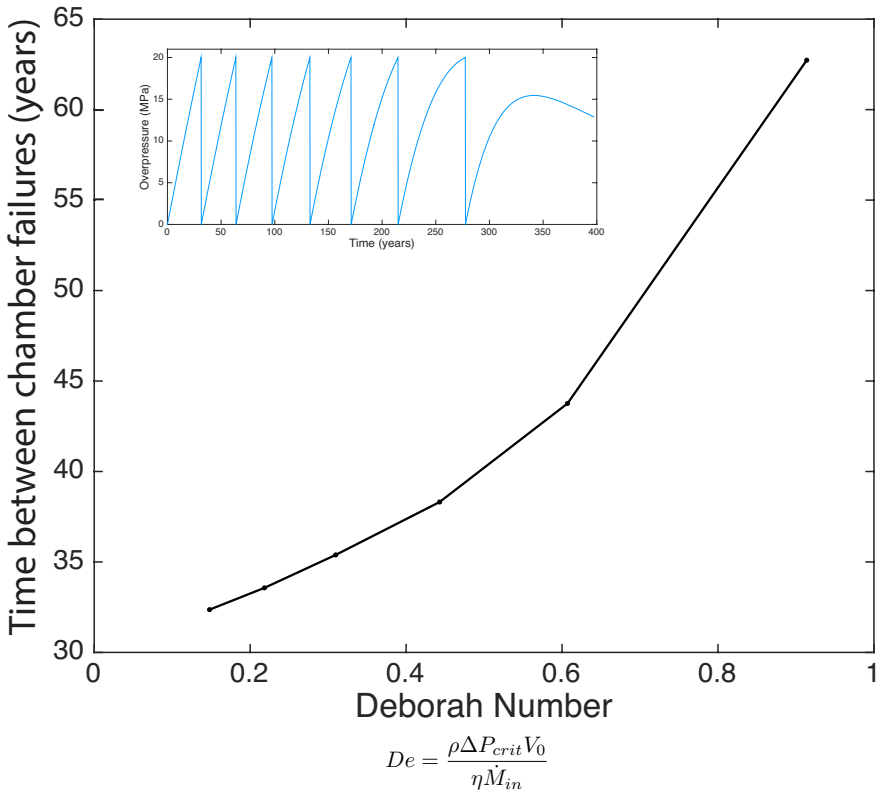

FIGURE 8. Time between chamber failures plotted against Deborah number. As the chamber approaches a Deborah number of 1 and the viscoelastic transition, the time between chamber failures increases. Black dots represent chamber failures. Inset shows the corresponding overpressure associated with the model run. The simulation had a 12km chamber depth, influx rate of 60 kgs^{-1}, and initial volume of 8 km^3.

Chemical Results

It is not known how chemical evolution of a magma chamber responds to thermo-mechanical cyclic failures, such as modeled in Figures (5-8). We model chemical evolution of the melt as one-way coupled to the thermo-mechanical processes. The evolution of concentration is sensitive to the partition coefficient, D, crustal concentrations, C_{WR}, and rates of recharge, evacuation, crystallization, and assimilation. Matching the findings of Lee et al. (2013), our model predicts an increase in time to steady state compositions for increasingly incompatible elements with partition coefficients less than one, as seen in Figure (9). In the simplest version of the Lee et al. (2013) model (which is essentially

identical to DePaolo (1981)), rates of mass transfer and chamber volume are held constant and thus mass cycling through the system results in a numerical steady state being reached in time. Our model concentrations approximate this behavior, but a numerical steady state is not reached because the rates of evacuation, crystallization, and assimilation are continuously changing throughout the simulations as the chamber progressively exhibits failure cycles and freezes. As the chamber heats up the surrounding crust, it insulates the chamber, reducing the efficiency of conduction at the boundary. This manifests as a decrease in crystallization rates as the chamber evolves. The most notable case is when the chamber crosses the viscoelastic transition. The steady state composition that the element concentrations relax to changes with the termination of chamber failures. Two important implications come from these observations. First, at time of chamber failure, a compatible element is much more likely to be at steady state composition than a highly incompatible element. Second, prolonged periods of steady state compositions may not occur due to the variability inferred for natural systems. Further research may yield a method for predicting the temporal history of a chamber through analysis of erupted packages and where elements are in their evolution towards steady state. This would allow for the tracking of changes in recharge, crystallization and assimilation rates prior to eruptions. Still, even in this framework, it is clear that magma compositions are a strong function of chamber mechanical regime through time.

Overturns, $\Delta\overline{M}_{re}$, are a unit defined in Lee et al. (2013) by the number of times cumulative recharge mass, ΔM_{re}, equals the chamber mass, M_{ch}, as shown in equation (3.6). The cycling of mass in Lee et al. (2013) is used as a proxy for the passage of time. Time and the evolution of melt density and volume fraction are used in the definition of an overturn in our model (equation 3.7). We use initial chamber volume for overturn calculations because in a viscoelastic regime, the chamber mass continuously grows with recharge and no overturns would be achieved. Since our model considers instantaneous homogenization of materials within the chamber, important zonation and intra-chamber dynamics may have a major affect on the path to steady state compositions. However,

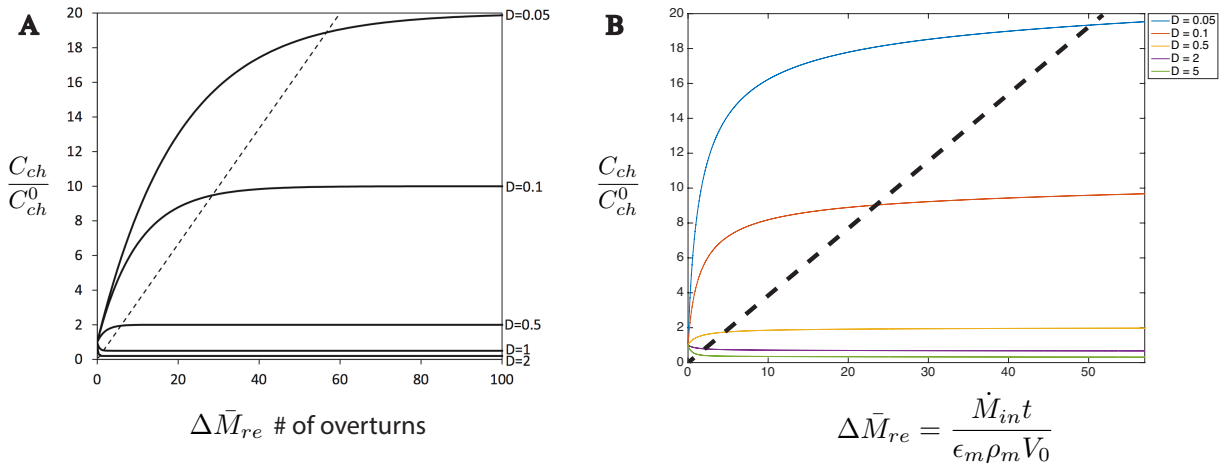

FIGURE 9. Overturns to steady state composition for a range of compatible and incompatible elements. A comparison of results from Lee et al. (2013) (Panel A) and our model (Panel B) is made. It takes longer to reach steady state compositions for incompatible elements, and significant changes in crystallization or evacuation rates can reset the steady state compositions that concentration is relaxing towards. Panel B is run for a chamber at 30 km depth, recharge rate of 350 kgs^{-1}, and initial volume of 5e7 m^3.

over long timescales, chambers that exhibit mixing of recharge and assimilation sourced magmas should behave similarly to our findings.

$$\Delta\overline{M}_{re} = \frac{\Delta M_{re}}{M_{ch}} \tag{3.6}$$

$$\Delta\overline{M}_{re} = \frac{\dot{M}_{in}t}{\epsilon_m \rho_m V_0} \tag{3.7}$$

Figure (10) explores the controls on whether steady state is reached before the chamber freezes. The mathematical definition of steady state is when the time derivative is equal to zero, $\frac{dC_m}{dt} = 0$. Since rates of crystallization, assimilation, and evacuation are not constant in our model, a mathematical steady state cannot be established and we use a threshold to define a quasi-steady state. We consider changes within the threshold of 5e-12 units of concentration per second averaged over a year to be steady state. Filled circles represent chamber simulations that reached steady state, and open circles did not reach steady state before freezing. As with Figure (9), it is rare for incompatible elements

to reach steady state concentrations before the chamber freezes, in contrast to compatible elements.

In panel A, mean crystallization rates are plotted in color. For the incompatible element, partition coefficient D=0.5, there are few chambers that reach steady state, all with the highest crystallization rates. The compatible elements, partition coefficients D=2 and D=5, expand the region of steady state into lower rates of crystallization. However, a few chambers in the upper right corner of the panels reach steady state before freezing, despite having low rates of crystallization. These are the chambers that are dominated by evacuation, as seen in Panel B. Average evacuation rates, plotted in color, increase towards the upper right corner. In Panel C, the ratio of averaged evacuation rates to crystallization rates are plotted in color. This demonstrates that the chambers in the upper right corner are evacuation driven, rather than crystallization driven. Assimilation and rates of recharge also have an impact on reaching compositional steady state, however, they are not shown in these panels. We are still in the processes of creating a predictive relationship for compositional steady state with respect to thermo-mechanical parameters.

We see two compositional steady state regimes that have emerged from these plots. 1) The fractional crystallization dominated regime is characterized by large chamber volumes and a viscoelastic thermo-mechanical regime. These chambers are also mobile for the longest amount of time before freezing, giving some incompatible elements the necessary time to reach steady state. The initial geotherm that the chamber is emplaced into affects this steady state regime by increasing the time before freezing, allowing more elements to reach steady state despite the lower rates of crystallization. 2) The evacuation dominated regime is characterized by smaller chamber volumes above or near the viscoelastic transition. These chambers are in the elastic thermo-mechanical regime. Crystallization still plays a role, but the averaged rate of evacuation is much larger. It is not as clear what other controls are influencing the path to steady state in this regime. The steady state chambers do not correlate perfectly with the highest ratios of

evacuation to crystallization rates, so assimilation and recharge rates could play a larger relative role in this regime. A cold initial geotherm or a shallow chamber depth would increase evacuation rates, however, these would also increase the rate of crystallization and decrease the rate of assimilation, so it is unclear at this time if this would increase the likelihood of steady state or inhibit it.

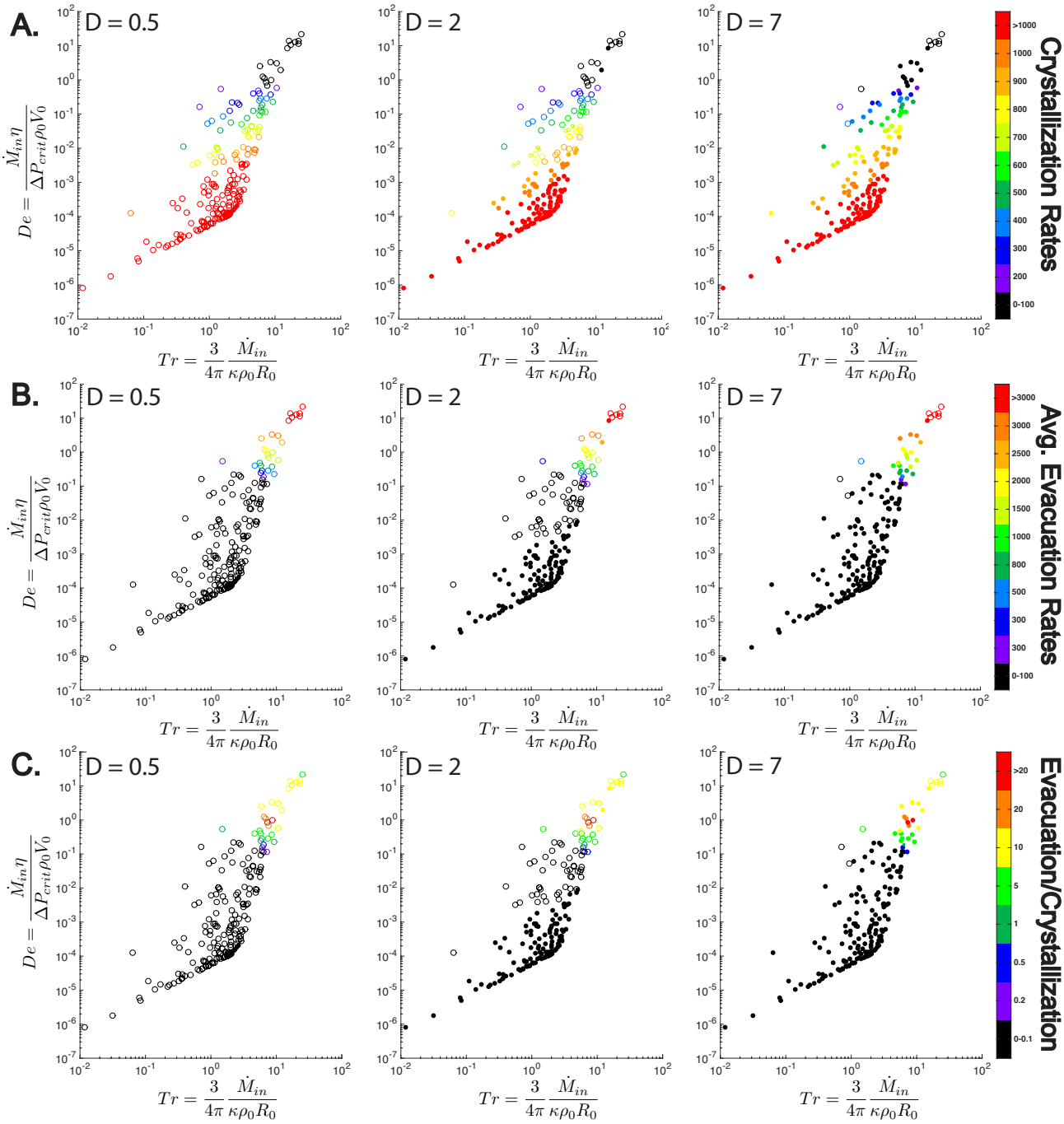

FIGURE 10. Plots of chambers that reached steady state compositions before freezing (filled circles) for partition coefficients D=0.5, 2, and 7. Recharge rates sampled between 0.01-100 kgs^{-1} and semi-minor axis length of 50-1000m at a depth of 15km. A) Averaged crystallization rates plotted in color. Higher crystallization rates tend to reach steady state first. B) Averaged evacuation rates plotted in color. C) Ratio of evacuation to crystallization rates plotted in color.

CHAPTER IV

CONCLUSIONS

The geophysical constraints on magmatic processes at depth are poorly understood. Our model acts as a physically and chemically consistent tool that can be compared to multi-faceted datasets collected at the surface, allowing us to learn about these poorly constrained processes that cause complexity. This gives us insight into the periods of quiescence and chamber growth, the periods of instability and chamber failure, what influences these regimes, and how they in turn affect the chemical composition of the magma. Magma chambers are an integral step in the magmatic transport system and our model provides a framework with which to explore these chambers and predict future trends and instabilities of active volcanic systems.

Our self-consistent model couples the thermo-mechanical and chemical processes that are important in influencing the evolution of a magma chamber. We predict stable and unstable regimes that give insight into the growth, storage, and death of magma chambers. If initial chamber volume is large enough or the surrounding crust is sufficiently pre-heated through prior magmatism, the viscoelastic transition can be reached. Relaxation of overpressure allows for the growth of long-lived and large chambers that remain stable over time (Karlstrom et al., 2010). The model considers constant recharge rates, however, a variable recharge rate may be required to first build large chambers of melt and crystal mush and then reanimate them to trigger caldera forming eruptions (Klemetti and Clynne, 2014; Degruyter et al., 2016).

We explore the increase in repose time between chamber failures as the viscoelastic transition is approached. This is a product of the thermal maturation of the crust. As the crust heats, viscosity drops around the chamber and it takes longer to pressurize. Future research on this topic may provide a more informed predictive tool for recurrence intervals at volcanic centers, however, variation in recharge rates and evolving crustal strength may influence or mask this phenomena in a natural system.

Additionally, our model can be used to predict the chemical evolution of an element in the melt phase - the first model to self consistently predict physical and chemical magma evolution through eruption cycles. We see a progression of element concentrations towards a steady state composition, which is influenced greatly by the rates of crystallization, evacuation, and assimilation. Compositions relax to a new steady state if significant change in rates occur, such as turning off chamber failures at the viscoelastic transition. The model predicts an increasing time to steady state composition for increasingly incompatible elements. The comparison of elements in steady state to those that are not at steady state compositions at time of eruption and their evolution between eruptive packages may provide insight into the processes of interest that influence the varying sizes and compositions of eruptions reaching the surface.

Yu et al. (2015) look at the compositional evolution at Large Igneous Provinces, such as the Columbia River Flood Basalts. The trends in nickel and potassium oxide concentration, a highly compatible and incompatible element in basaltic magmas respectively, are complex and vary between enrichment and depletion throughout the deposited layers. When nickel is depleted, potassium oxide is enriched, pointing towards a fractional crystallization dominated chamber environment before eruption and when the opposite occurs, a recharge dominant chamber environment is implied. However, nickel only varies over a window of 85 ppm and potassium oxide varies over 16,000 ppm, a much larger window. Our model results demonstrate a similar behavior. The steady state composition of a compatible element does not vary on the same scale seen with incompatible elements and reaches that steady state composition in a much shorter amount of time. This means that variations due to changing crystallization and recharge rates will produce smaller windows of variation and the compositions erupted are much more likely to be that of steady state for a compatible element. On the other hand, incompatible elements vary over a large window of concentrations, especially during periods of fractional crystallization, and are much less likely to have reached steady state when an eruption occurs. An in depth study on the concentration changes of a

compatible element, such as nickel, could be used to infer the new rates of recharge, crystallization, and assimilation. The relative rates of change between a compatible and incompatible element, such as potassium oxide, could indicate where the incompatible element was on its path to steady state. This could act as a proxy for temporal history of the changing rates, giving us a better idea of the timeline and magnitude of recharge events and major shifts in chamber evolution leading to eruption.

Future Directions

The immediate future of the project is to address some inconsistencies between the model and natural systems. Although a decent proxy for a deep chamber, neglecting volatiles in the system is not physical, especially since they play a large role in the compressibility of melts and the pressurization of a chamber. Volatiles are also a major trigger for chamber failure through second boiling (Fowler and Spera, 2008, 2010). Adding in a solubility model for volatiles, mainly water and carbon dioxide, is an important future step for this model.

Another inconsistency in the model is that the evolution of chemical composition does not influence the thermo-mechanical processes. A true two way couple should be established to improve the consistency of the model. The chemical composition of the melt should impact the crystallization rates through the power law exponent in the crystal volume fraction calculation, liquidus and solidus temperatures, and latent heat of crystallization.

Since the temperature in the crust is solved for on a variable grid, taking into account the moving boundary conditions, the model can be used to explore the effects of linking multiple chambers together. Evidence in petrologic and seismic studies has pointed towards systems of linked chambers and mixing of melts with varying crustal contaminations. As such, it would be informative to compare model outputs for a series of linked chambers to surface data to see if a unique solution to processes happening at

depth exists, or if many different paths can be taken to produce the data patterns seen at the surface.

Finally, to really understand what is going on at depth and constrain rates and magnitudes of magmatic processes, a comparison to surface data must be made. Through formal inversion methods, we can compare model output to the time between eruptions, volumes and compositions of erupted materials, and depth estimates from melt inclusions and seismic data seen at volcanic centers (Figure 2). This will identify the system controls that can be well constrained through observations at the surface and give us a better understanding of what happens at depth below the volcanic edifice.

APPENDIX

HEAT EQUATION ON A TIME-VARYING DOMAIN

Transforming the variable domain caused by a moving chamber boundary onto a fixed domain allows us to solve the heat equation for the thermal evolution in the crust. The diffusion equation is as follows, where Θ is the temperature in the crust, κ is the thermal diffusivity, and z the distance from the chamber.

$$\frac{\partial \Theta}{\partial t} = \kappa \frac{\partial^2 \Theta}{\partial z^2}, \quad z_1(t) \leq z \leq z_2(t) \tag{A.1}$$

$$\text{Initial condition: } \Theta(0, z) = \Theta_0(z)$$

$$\text{Left boundary condition: } \Theta(t, z_1(t)) = \Theta_L(t)$$

$$\text{Right boundary condition: } \Theta(t, z_2(t)) = u_R(t)$$

The interval $z_1(t) \leq z \leq z_2(t)$ is mapped to the fixed domain $0 \leq \xi \leq 1$ through the transformation

$$\xi = \frac{z - z_1(t)}{z_2(t) - z_1(t)}, \tag{A.2}$$

with inverse mapping

$$z = \xi(z_2(t) - z_1(t)) + z_1(t). \tag{A.3}$$

Time is transformed via $\tau = t$, to make calculations more straight forward. Partial derivative operators are then

$$\frac{\partial}{\partial z} = \frac{\partial \xi}{\partial z}\frac{\partial}{\partial \xi} + \frac{\partial \tau}{\partial z}\frac{\partial}{\partial \tau} = \frac{1}{z_2 - z_1}\frac{\partial}{\partial \xi}, \tag{A.4}$$

$$\frac{\partial^2}{\partial z^2} = \frac{1}{(z_2 - z_1)^2}\frac{\partial^2}{\partial \xi^2}, \tag{A.5}$$

and

$$\frac{\partial}{\partial t} = \frac{\partial \xi}{\partial t}\frac{\partial}{\partial \xi} + \frac{\partial \tau}{\partial t}\frac{\partial}{\partial \tau} = \dot{\xi}\frac{\partial}{\partial \xi} + \frac{\partial}{\partial \tau}, \tag{A.6}$$

where a dot indicates a time derivative and $\dot{\xi}$ is defined as

$$\dot{\xi} = \frac{-\dot{z}_1 - \xi(\dot{z}_2 - \dot{z}_1)}{(z_2 - z_1)}. \tag{A.7}$$

Applying these transformed derivative operators we arrive at the transformed heat equation. Notice that an advection term has been added as a consequence of the moving boundary.

$$\frac{\partial \Theta}{\partial \tau} = -\dot{\xi}\frac{\partial \Theta}{\partial \xi} + \kappa \frac{1}{(z_2 - z_1)^2}\frac{\partial^2 \Theta}{\partial \xi^2}, \quad 0 \leq \xi \leq 1 \tag{A.8}$$

$$\text{Initial condition: } \Theta(0, \xi) = \Theta_0(\xi)$$

$$\text{Left boundary condition: } \Theta(\tau, 0) = \Theta_L(\tau)$$

$$\text{Right boundary condition: } \Theta(\tau, 1) = \Theta_R(\tau)$$

REFERENCES CITED

Anderson, K. and Segall, P. (2011). Physics-based models of ground deformation and extrusion rate at effusively erupting volcanoes. *Journal of Geophysical Research: Solid Earth*, 116(B7):n/a–n/a. B07204.

Annen, C. (2009). From plutons to magma chambers: Thermal constraints on the accumulation of eruptible silicic magma in the upper crust. *Earth and Planetary Science Letters*, 284(3):409 – 416.

Asimow, P. and Ghiorso, M. (1998). Algorithmic modifactions extending melts to calculate subsolidus phase relations. *American Mineralogist*, 83:1127–1131.

Barry, T., Kelley, S., Reidel, S., Camp, V., Self, S., Jarboe, N., Duncan, R., and Renne, P. (2013). Eruption chronology of the columbia river basalt group.

Bergantz, G. (1989). Underplating and partial melting: Implications for melt generation and extraction. *Science*, 245(4922):1093–1095.

Blake, S. (1984). Volatile oversaturation during the evolution of silicic magma chambers as an eruption trigger. *Journal of Geophysical Research*, 89:8237–8244.

Caricchi, L., Annen, C., Blundy, J., Simpson, G., and Pinel, V. (2014). Frequency and magnitude of volcanic eruptions controlled by magma injection and buoyancy. *Nature Geosci*, 7(2):126–130.

Cervantes, P. and Wallace, P. (2003). Role of h2o in subduction-zone magmatism: New insights from melt inclusions in high-mg basalts from central mexico. *Geology*, 31(3):235–238.

Cervelli, P. (2013). Analytical expression for deformation from an arbitrarily oriented spheroid in a half-space. *Eos, Transactions American Geophysical Union*.

Defant, M. and Kepezhinskas, P. (2001). Evidence suggests slab melting in arc magmas. *Eos, Transactions American Geophysical Union*, 82(6):65–69.

Degruyter, W. and Huber, C. (2014). A model for eruption frequency of upper crustal silicic magma chambers. *Earth and Planetary Science Letters*, 403:117–130.

Degruyter, W., Huber, C., Bachmann, O., Cooper, K., and Kent, A. (2016). Magma reservoir response to transient recharge events: The case of santorini volcano (greece). *Geology*, 44(1):23–26.

DePaolo, D. (1981). Trace element and isotopic effects of combined wallrock assimilation and fractional crystallization. *Earth and Planetary Science Letters*, 53(2):189–202.

Dragoni, M. and Magnanensi, C. (1989). Displacement and stress produced by a pressurized, spherical magma chamber, surrounded by a viscoelastic shell. *Physics of the Earth and Planetary Interiors*, 56:316–328.

Dungan, M. and Rhodes, J. (1978). Residual glasses and melt inclusions in basalts from dsdp legs 45 and 46: Evidence for magma mixing. *Contributions to Mineralogy and Petrology*, 67(4):417–431.

Fowler, S. and Spera, F. (2008). Phase equilibria trigger for explosive volcanic eruptions. *Geophysical Research Letters*, 35(8):n/a–n/a. L08309.

Fowler, S. and Spera, F. (2010). A metamodel for crustal magmatism: phase equilibria of giant ignimbrites. *Journal of Petrology*, 0(0):1–48.

Ghiorso, M. and Sack, O. (1991). Fe-ti oxide geothermometry: thermodynamic formulation and the estimation of intensive variables in silicic magmas. *Contributions to Mineralogy and Petrology*, 108(4):485–510.

Ghiorso, M. and Sack, O. (1995). Chemical mass transfer in magmatic processes iv. a revised and internally consistent thermodynamic model for the interpolation and extrapolation of liquid-solid equilibria in magmatic systems at elevated temperatures and pressures. *Contributions to Mineralogy and Petrology*, 119:197–212.

Gregg, P., de Silva, S., Grosfils, E., and Parmigiani, J. (2012). Catastrophic caldera-forming eruptions: Thermomechanics and implications for eruption triggering and maximum caldera dimensions on earth. s 241–242:1–12.

Gudmundsson, A. (2006). How local stresses control magma-chamber ruptures, dyke injections, and eruptions in composite volcanoes. 79:1–31.

Gudmundsson, A. (2012). Magma chambers: Formation, local stresses, excess pressures, and compartments. *Journal of Volcanology and Geothermal Research*, 237-238:19–41.

Gudmundsson, A., Marti, J., and Turon, E. (1997). Stress fields generating ring faults in volcanoes. *Geophysical Research Letters*, 24(13):1559–1562.

Hales, T. C., Abt, D. L., Humphreys, E. D., and Roering, J. J. (2005). A lithospheric instability origin for columbia river flood basalts and wallowa mountains uplift in northeast oregon. *Nature*, 438(7069):842–845.

Hill, E., Brittain, Connor, C., S. Jarzemba, M., La Femina, P., Navarro, M., and Strauch, W. (1998). 1995 eruptions of cerro negro volcano, nicaragua, and risk assessment for future eruptions. 110:1231–1241.

Huber, C., Bachmann, O., and Manga, M. (2009). Homogenization processes in silicic magma chambers by stirring and latent heat buffering. *Earth and Planetary Science Letters*, 283:38–47.

Jellinek, A. and DePaolo, D. (2003). A model for the origin of large silicic magma chambers: precursors of caldera-forming eruptions. *Bulletin of Volcanology*, 65(5):363.

Johnson, C. and Rutherford, M. (1989). Experimental calibration of the aluminum-in-hornblende geobarometer with applicable to long valley caldera (california) volcanic rocks. 17:837–841.

Karlstrom, L., Dufek, J., and Manga, M. (2010). Magma chamber stability in arc and continental crust. *Journal of Volcanology and Geothermal Research*, 190(3):249–270.

Karlstrom, L., Paterson, S., and Jellinek, A. (2017). A reverse energy cascade for crustal magma transpor. *Nature Geoscience*, 10(8):604–608.

Klemetti, E. and Clynne, M. (2014). Localized rejuvenation of a crystal mush recorded in zircon temporal and compositional variation at the lassen volcanic center, northern california. *PLOS One*, 9(12).

Lee, C., Lee, T., and Wu, C. (2013). Modeling the compositional evolution of recharging, evacuating, and fractionating (refc) magma chambers: Implications for differentiation of arc magmas. *Geochimica et Cosmochimica Acta*, 143:8–22.

Lister, J. and Kerr, R. (1991). Fluid-mechanical models of crack propagation and their application to magma transport in dykes. *Journal of Geophysical Research: Solid Earth*, 96(B6):10049–10077.

Marsh, B. (1982). On the mechanics of igneous diapirism, stoping, and zone melting. *American Journal of Science*, 282:808–855.

Paterson, S., Okaya, D., Memeti, V., Economos, R., and Miller, R. (2011). Magma addition and flux calculations of incrementally constructed magma chambers in continental margin arcs: Combined field, geochronologic, and thermal modeling studies. *Geosphere*, 7:1439–1468.

Reidel, S., Camp, V., Tolan, T., and Martin, B. (2013). The columbia river flood basalt province: Stratigraphy, areal extent, volume, and physical volcanology. *Geological Society of America Special Papers*, 497:1–43.

Rivalta, E., Bottinger, M., and Dahm, T. (2005). Buoyancy driven fracture ascent: Experiments in layered gelatine. *Journal of Volcanology and Geothermal Research*, 144:1–4.

Rubin, A., Cooper, K., Till, C., Kent, A., Costa, F., Bose, M., and Gravley, D. (2017). Rapid cooling and cold storage in a silicic magma reservoir recorded in individual crystals. *Science*, 356(6343):1154–1156.

Segall, P. (2016). Repressurization following eruption from a magma chamber with a viscoelastic aureole. *Journal of Geophysical Research: Solid Earth*, 121:8501–8522.

Sibik, S., Edmonds, M., Maclennan, J., and Svensen, H. (2015). Magmas erupted during the main pulse of siberian traps volcanism were volatile-poor. *Journal of Petrology*, 56(11):2089–2116.

Sigmarsson, O. (1996). Short magma chamber residence time at an icelandic volcano inferred from u-series disequilibria. 382:440–442.

Spera, F. and Bohrson, W. (2004). Open-system magma chamber evolution: an energy-constrained geochemical model incorporating the effects of concurrent eruption, recharge, variable assimilation and fractional crystallization (ec-e'raxfc). *Journal of Petrology*, 45(12):2459–2480.

Wallace, P. (2004). Volatiles in subduction zone magmas: concentrations and fluxes based on melt inclusion and volcanic gas data. *Journal of Volcanology and Geothermal Research*, 140:217–240.

Wolff, J., Ramos, F., Hart, G., Patterson, J., and Brandon, A. (2008). Columbia river flood basalts from a centralized crustal magmatic system. *Nature Geoscience*, 1:177–180.

Yu, X., Lee, C., Chen, L., and Zeng, G. (2015). Magmatic recharge in continental flood basalts: Insights from the chifeng igneous province in inner mongolia. *Geochemistry, Geophysics, Geosystems*, 16(7):2082–2096.